Effects of SiO$_2$ interlayers on the phase change behavior in the multilayer Zn$_{15}$Sb$_{85}$/SiO$_2$ materials

Rui Zhang [a], Yifeng Hu [a, c, d, *], Qingqian Chou [b], Tianshu Lai [b, **], Xiaoqin Zhu [a]

[a] School of Mathematics and Physics, Jiangsu University of Technology, Changzhou 213000, China
[b] State-Key Laboratory of Optoelectronic Materials and Technology, School of Physics, Sun Yat-Sen University, Guangzhou 510275, China
[c] State Key Laboratory of Silicon Materials, Zhejiang University, Hangzhou 310027, China
[d] Key Laboratory of Semiconductor Materials Science, Beijing Key Laboratory of Low Dimensional Semiconductor Materials and Devices, Institute of Semiconductors, Chinese Academy of Sciences, Beijing, 100083, China

ARTICLE INFO

ABSTRACT

In this study, the multilayer Zn$_{15}$Sb$_{85}$/SiO$_2$ materials were investigated for phase change memory application with the intention of improving thermal stability and switching speed. The Zn$_{15}$Sb$_{85}$/SiO$_2$ materials exhibited a high crystallization temperature (T_c~230 °C), good data retention (T_{10} ~ 160 °C), small density change (~3.3%), flat surface and rapid amorphization speed (~1.34 ns). T-shaped phase change devices based on Zn$_{15}$Sb$_{85}$/SiO$_2$ materials achieved low RESET voltage (V_{RESET} ~1.3 V) in programming operation. The results showed that the multilayer Zn$_{15}$Sb$_{85}$/SiO$_2$ material was a promising phase change material with high thermal ability, low power consumption and rapid switching speed.

© 2019 Elsevier B.V. All rights reserved.

1. Introduction

With the great development of electronic information technology and the universalization of the mobile Internet, the human society has entered the era of big-data. The trend of data growth becomes more and more obvious, which results in a large variety kinds of information need to be recorded, stored, transmitted and processed. So, the development of electronic memory devices is facing a tremendous challenge [1]. The demand for non-volatile memory devices with high density, fast speed and low-power consumption is becoming more and more urgent [2]. On the other hand, the huge breakthroughs of artificial intelligence (AI) technology will play a leading role in the future technological revolution and promote the development of the information era, which have caused widespread concern. Both the big-data era and AI developments bring up a new and higher requirements for the hardware of processor and memory, namely, breaking the Von Neumann bottleneck. So, electronic memory is a key technology to

deal with the big-data storage and will play a central role in the development of information technology [3]. As an emerging non-volatile memory technology, the phase-change memory (PCM) is possible to substitute both the dynamic random access memory and flash memory, and thus serves as the universal memory [4]. Now, the PCM devices show excellent performances, such as smaller device size, better compatibility, longer life and excellent anti-irradiation property which are close to commercial application. However, there are still some insufficiencies in the performance of PCM, such as high power consumption and poor data retention at high temperature. The recording speed, density and cyclability of PCM have a lot of room for improvement, as well [5—7].

The phase change materials play a very important role in PCM. The doping is one of the most favoured ways of improving material performance by changing ingredient [8]. However, there is a contradiction between the data retention and phase change speed in PCM, which can not be solved by doping. A better thermal stability is usually at the expense of a slower speed. Recently, nano multilayer phase change materials have received increasing attention due to their ability to provide more control parameters (material thickness, periodicity, number of periodic cycles), in addition to composition [9,10]. The multilayer materials can

combine the advantages of different compositions to obtain better performance by increasing the reversible phase change speed and reducing the overall operating power consumption. In this study, we hope to make great improvements in the phase change materials to meet the requirements of next generation of memory [11—13]. So, the multilayer $Zn_{15}Sb_{85}/SiO_2$ (ZS/SO, for short) materials with various proportion were deposited by a sputtering method [14]. The effects of SiO_2 interlayers on $Zn_{15}Sb_{85}$ materials were investigated systematically, including the phase change behavior, thermal properties, phase structure, crystallization mechanism and electrical switching characteristics of PCM devices [15,16].

2. Experiments

The amorphous multilayer $[ZS(a)nm/SO(10-a)nm]_5$ (a = 3, 5, 7) and monolayer ZS materials with a total thickness of 50 nm were deposited on SiO_2/Si (100) substrate at room temperature by a radio-frequency magnetron sputtering system with $Zn_{15}Sb_{85}$ and SiO_2 targets, respectively. The targets with the purity of 99.999% were carefully cleaned before sputtering. The thickness of the materials were adjusted by controlling the sputtering power, working pressure and deposition time. Alternating current power was set at 30 W, and the deposition time was determined by the sputtering rate. The background pressure was lower than 2.0×10^{-4} Pa and the deposition pressure was set at 4×10^{-1} Pa. An automatic rotation of 20 revolutions per minute (rpm) for the substrate was used to guarantee a uniform deposition. All the sputtering operations above were carried out in an Ar atmosphere with a flow rate of 30 sccm. The specific parameters of sputtering were shown in Table 1.

The dependence of the resistance on the temperature (R—T) of the multilayer ZS/SO and monolayer ZnSb materials were measured *in situ* in a homemade vacuum chamber with a TP 94 temperature controller (Linkam Scientific Instruments Ltd, Surrey, UK). The data retention ability of the amorphous state was estimated. Diffuse reflectance spectra were recorded by a near infrared spectroscopy (NIR, 7100CRT, XINMAO, China) spectrophotometer in the wavelength range of 400—2500 nm. The crystalline phase structure was analyzed by X-ray diffraction (XRD, PANalytical, X'PERT Powder) with Cu Kα radiation in the 2θ range from 20° to 60° performed at 40 kV and 50 mA. The surface morphology of the PCM cells was observed by atomic force microscopy (AFM, FM-Nanoview 1000). The real-time reflectivity measurement was tested by a picosecond laser pump-probe system. The light source used for irradiating the samples was a frequency-doubled model-locked neodymium yttrium aluminum garnet laser with the operating wave-length 532 nm and pulse duration 30 ps The volume change during the crystallization process was determined by x-ray reflectivity (XRR). T-shaped PCM devices were manufactured to confirm the electrical switching characteristics. The current-voltage (I-V) and resistance-voltage (R-V) properties were recorded using an arbitrary waveform generator (Tektronix AWG5012B) and a digital semiconductor parameter analyzer (Keithley 2602A).

3. Results and discussion

Fig. 1 shows R-T curves for multilayer ZS/SO and monolayer ZS materials at the heating rate of 20 °C/min. The schematic diagram of ZS/SO multilayer structure was displayed in the inset. The green and blue squares in the illustration represent the wafer. Meanwhile, the yellow squares represent the ZnSb film materials and the red squares represent the SiO_2 materials, both of which are prepared by magnetron sputtering. The resistance of multilayer ZS/SO materials decreases slowly at the beginning and declines sharply when the temperature reaches T_c (phase change temperature). The high resistance before the T_c refers to the disordered amorphous state. In the contrast, the low resistance state after the T_c is recognized as the ordered crystalline state. The resistance ratio between amorphous and crystalline states for ZS/SO is over one order of magnitude, which can meet the requirement of PCM [18]. As shown in the Fig. 1, the T_c of ZS is around 185 °C. With the increasing proportion of SiO_2, the T_c for $[ZS(7 nm)/SO(3 nm)]_5$, $[ZS(5 nm)/SO(5 nm)]_5$, $[ZS(3 nm)/SO(7 nm)]_5$ are 205 °C, 210 °C, 230 °C, respectively. Compared with GST (170 °C for T_c) [19], the multilayer ZS/SO materials have obvious advantages. In terms of improving thermal stability in multilayer materials, the layer with higher T_c plays a leading role. At the same time, the amorphous resistance for ZS, $[ZS(7 nm)/SO(3 nm)]_5$, $[ZS(5 nm)/SO(5 nm)]_5$, $[ZS(3 nm)/SO(7 nm)]_5$ are 6.8×10^5, 2.0×10^6, 4.5×10^6 and 8.2×10^6 Ω, respectively. According to the formula:

$$Q = I^2 \times R \times t \tag{1}$$

A better self-heating efficiency can be achieved with a higher resistance, which will result in a decrease of power consumption in current induced resistance switching [19].

Fig. 2 shows the band gap energy (E_g) which can be determined by extrapolating the absorption edge onto the energy axis. Here the conversion of the reflectivity to absorbance data is obtained by the Kubelka-Munk function (K-M) [20]:

$$K/S = (1 - R)(1 - R)^2 / (2R) \tag{2}$$

where R is the reflectivity, K is the absorption coefficient, and S is the scattering coefficient. Fig. 2 shows that the E_g decreases after crystallization for both monolayer ZS and multilayer $[ZS(3 nm)/SO(7 nm)]_5$ materials. The values of E_g for ZS(amorphous) and ZS(crystalline) are 2.85 and 2.80 eV, respectively. Similarly, the E_g for $[ZS(3 nm)/SO(7 nm)]_5$ decreases from 2.86 to 2.84 eV after annealing. The difference for E_g is related to the carrier concentration in phase change materials. Because the carrier density inside the semiconductors is proportional to Ref. exp $(-E_g/2KT)$ [18]. A broad band gap will increase the obstacle of carrier transition, leading to the increase of resistivity. After the SiO_2 layers are added, the E_g is also broadened. This finding supports the conclusions of resistance curves in Fig. 1 [21].

The values of slope B and U for the monolayer ZS and the multilayer $[ZS(3 nm)/SO(7 nm)]_5$ materials were determined from

Table 1
Specific parameters of magnetron sputtering.

Serial Number	Sample Composition	$Zn_{15}Sb_{85}$(Target A)		SiO_2(Target B)		Aggregate Thickness/nm
		Thickness/nm	Sputtering Time/s	Thickness/nm	Sputtering Time/s	
1	ZS	50	125	0	0	50
2	$[ZS(7 nm)SO(3 nm)]_5$	7	17.5	3	7	
3	$[ZS(5 nm)GS(5 nm)]_5$	5	12.5	5	11	
4	$[ZS(3 nm)SO(7 nm)]_5$	3	7.5	7	16	

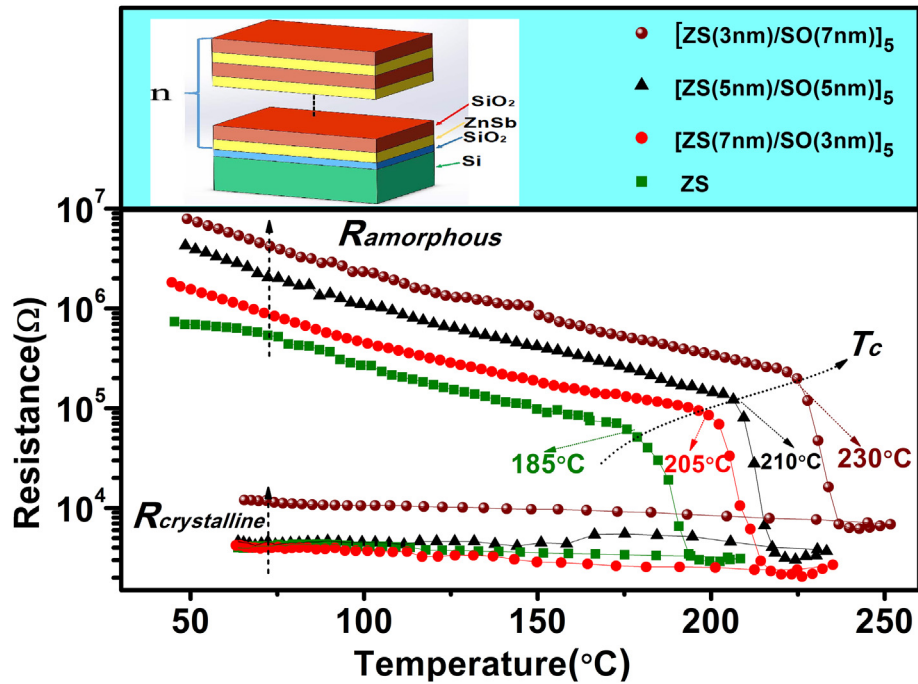**Fig. 1.** The resistance of the monolayer ZS (50 nm) and multilayer [ZS(a)nm/SO(10-a)nm]₅ (a = 3, 5, 7) materials as a function of temperature with a heating rate of 20 °C/min. Inset shows the schematic diagram of ZS/SO multilayer structure (Different colors represent different components). (For interpretation of the references to color in this figure legend, the reader is referred to the Web version of this article.)
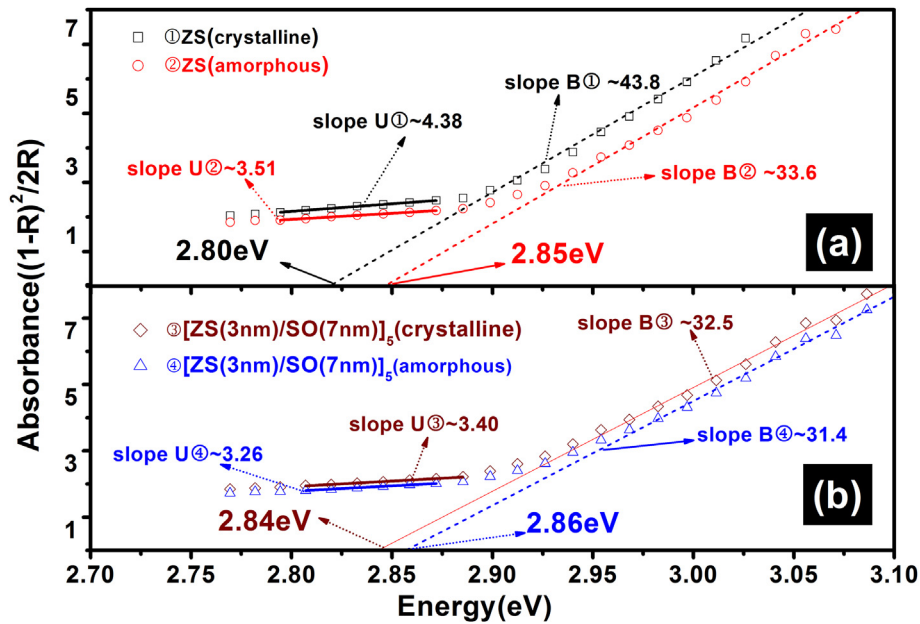

Fig. 2. The Kubelka−Munk function of **(a)** monolayer ZS materials. **(b)** The multilayer [ZS(3)nm/SO(7)nm]₅ materials.

Fig. 2. The increase for slope *B* is related to the reduction in randomness in atomic configuration. Slope *B*① (~43.8) is larger than that of Slope *B*② (~33.6). Obviously, the crystalline structure has more orderly atomic configuration than that of the amorphous structure. For the multilayer [ZS(3 nm)/SO(7 nm)]₅ materials, the same trend occurs with the increasing from Slope *B*④ (~31.4) to Slope *B*③ (~32.5). An increase in slope *U* is caused by the diminution of the band-tail localized states inside the material. The slope *U* for ZS (amorphous) and ZS(crystalline) are (slope *U*②~3.51) and

(slope *U*①~4.38), respectively. The change in the slope *U* of ZS indicates that the degree of crystallization of the materials becomes higher after annealing, and the degree of amorphous state is lowered. Likewise, the slope *U* has a slightly smaller increasing for the [ZS(3 nm)/SO(7 nm)]₅ from (slope *U*④~3.26) to (slope *U*③~3.40). The results illustrate that the degree of amorphous state is reduced and the crystallization process is suppressed by SiO₂ layers [22].

With the intention of further evaluating the thermal stability, the isothermal crystallization test was carried out. In this work, the

required time for the resistance decreasing to half of the amorphous value is defined as the failure time. For this purpose, all monolayer and multilayer materials were annealed at different temperatures. Then, the failure time is fitted to calculate the temperature at which the materials can work normally for 10 years. The plot of logarithm failure time versus $1/k_bT$, exhibited in Fig. 3 fits a linear Arrhenius relationship because of its thermal activation nature. The linear relationship is described as follows:

$$t = \tau_0 \exp [E_c/(k_b \times T)] \tag{3}$$

where t, τ_0, k_b, and T are failure time, a pre-exponential factor depends on the material properties, Boltzmann constant and absolute temperature, respectively [17]. Fig. 3 shows the estimated temperatures of 10-year data retention lifetime for the ZS, [ZS(7 nm)/SO(3 nm)]$_5$, [ZS(5 nm)/SO(5 nm)]$_5$, [ZS(3 nm)/SO(7 nm)]$_5$ are 113, 141, 151 and 160 °C, respectively. Meanwhile, the activation energy (E_a) of each material can be acquired from the slope of the straight line in the corresponding Arrhenius plots [23]. A larger E_a means that the materials is more difficult to crystallize which indicates that the thermal stability of the material is excellent as well. As shown in Fig. 3, the E_a of ZS, [ZS(7 nm)/SO(3 nm)]$_5$, [ZS(5 nm)/SO(5 nm)]$_5$, [ZS(3 nm)/SO(7 nm)]$_5$ are 3.68, 4.56, 4.83 and 5.73 eV. By comparing the results of GST (T_{10}~85 °C, E_a 2.28 eV), it can be found that the thermal stability of the ZS/SO is better than GST [24].

The phase structures of ZS and [ZS(3 nm)/SO(7 nm)]$_5$ materials were examined by XRD. Fig. 4 shows the XRD patterns of the materials after annealing at different temperatures for 25 min. In the Fig. 4 (a) and (b), no obvious diffraction peaks can be observed when the annealing temperature was under 150 °C. However, when the temperature rises up to 190 °C, the diffraction peak Sb (012) can be observed for both ZS and [ZS(3 nm)/SO(7 nm)]$_5$. In the Fig. 4 (a), as the annealing temperature increases from 190 to 300 °C, stronger diffraction peaks can be observed, indicating that crystallization of the monolayer materials become more and more obvious. Meanwhile, a new diffraction peak of Sb (110) is observed until the temperature rising to 240 °C. On the other hand, the diffraction

peaks of [ZS(3 nm)/SO(7 nm)]$_5$ materials do not have obvious change with the increase of annealing temperature. It indicates that the crystallization was inhibited by SiO$_2$ layers. We can calculate the grain size by using the Scherrer equation:

$$D_{hkl} = 0.943\lambda/\beta \cos \theta \tag{4}$$

D_{hkl} is the grain sizes, λ is the X-ray wavelength (0.1540 nm), β is the half-height width of the diffraction peak of the measured sample, θ is the Bragg diffraction angle, and the unit is angle (in degrees). From the main peak at around 28.5°, the grain sizes of annealed ZS and [ZS(3 nm)/SO(7 nm)]$_5$ are 21.3 and 18.5 nm, respectively. The results illustrate that the crystallization of [ZS(3 nm)/SO(7 nm)] is suppressed and the grains become smaller. After the recombination, the crystallization of the materials becomes more difficult, but the thermal stability of the amorphous state is also improved.

The surface roughness of the phase change materials has considerable impacts on the quality of the interface between the electrode and phase change material layer. Fig. 5 (a)~(d) exhibit the AFM images of as-deposited and crystallized ZS and [ZS(3 nm)/SO(7 nm)]$_5$ materials. For as-deposited ZS and [ZS(3 nm)/SO(7 nm)]$_5$ materials, the surface is relatively smooth, indicating distinct amorphous structure. After irradiating by high energy laser beam, a mass of grains can be observed. Compared with ZS in Fig. 5(b), the grains of [ZS(3 nm)/SO(7 nm)]$_5$ become more compact and smaller. The root-mean-square (RMS) surface roughness of ZS increases from 0.35 nm of as-deposited state to 109.5 nm of crystalline state. In contrast, the difference of RMS for [ZS(3 nm)/SO(7 nm)]$_5$ is only 35.65 nm before and after crystallization, which is much lower than that of ZS (109.15 nm). It can be deduced that the SiO$_2$ interlayers prevent the further growth of grains and guarantee the good interface contact, which is conducive to improve the fatigue performance of the PCM [25].

The phase change speed is an important feature of the PCM performances because it has a great effect on the switching performance of the PCM device. Accompanied by the phase change process, the optical reflectivity will have great changes. As shown in
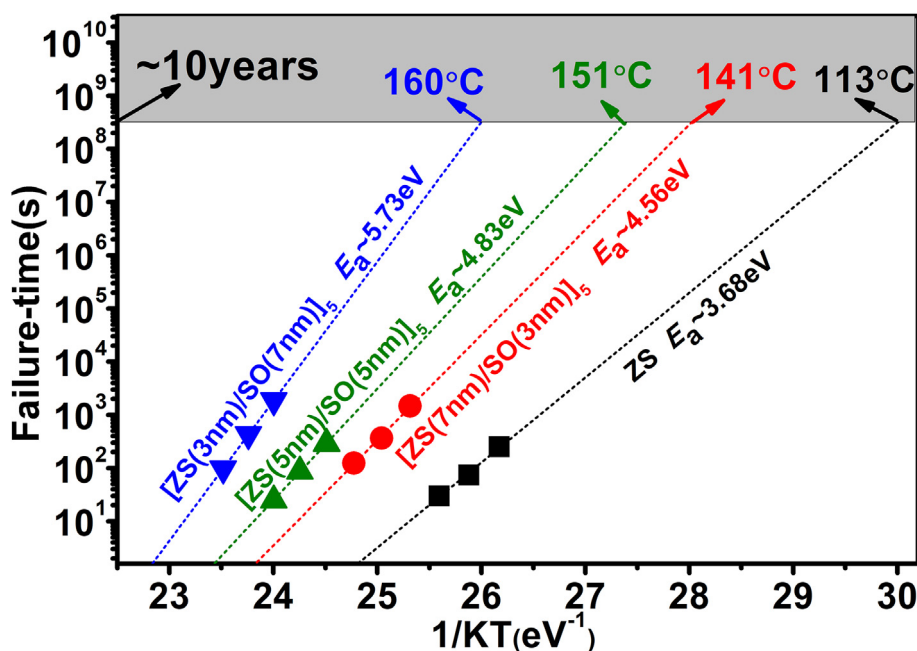

Fig. 3. Plot of failure time versus reciprocal temperature of ZS and multilayer [ZS(a)nm/SO(10-a)nm]$_5$ (a = 3,5,7) materials, showing the data retention temperature for 10 years and Arrhenius plots for E_a.
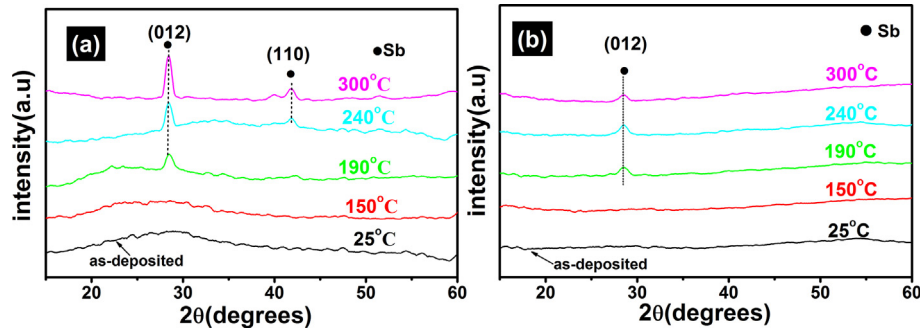
Fig. 4. (a) XRD patterns of monolayer ZS materials annealed at different temperatures for 25 min in Ar atmosphere. **(b)** XRD patterns of multilayer [ZS(3)nm/SO(7)nm]$_5$ materials annealed at different temperatures for 25 min in Ar atmosphere.
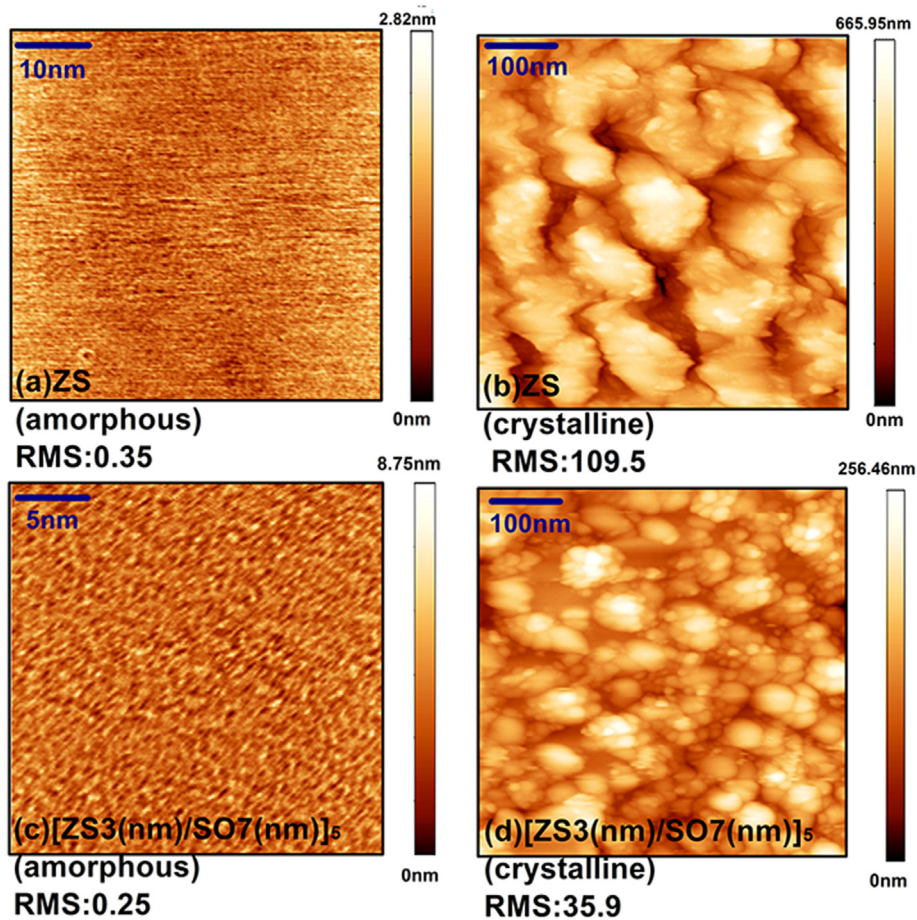

Fig. 5. AFM topographic images of as-deposited **(a)** ZS and **(c)** [ZS(3)nm/SO(7)nm]$_5$ materials; crystalline **(b)** ZS and **(d)** [ZS(3)nm/SO(7)nm]$_5$ materials irradiated by laser beam.

Fig. 6, a sudden rise in reflectivity is considered to be an amorphous-crystalline transformation. The crystalline multilayer materials are in a state with a high reflectivity and the amorphous multilayer materials are in a low reflectivity. After the irradiation of laser pulse, the heat generated by the pulse triggers the SET process of the materials, resulting in the increasing of the reflectivity. Therefore, we define the abrupt increase in reflectivity as the amorphous-to-crystalline phase transition. The results show that the time of ZS and [ZS(3 nm)/SO(7 nm)]$_5$ are 1.65 and 1.3 ns, respectively. It is reported that the GST material takes about 41 ns [26] to achieve the same switching. This indicates that [ZS(3 nm)/SO(7 nm)]$_5$ has a faster phase change rate than GST. In

Sb-rich Zn$_{15}$Sb$_{85}$ materials, a good deal of Sb phases exist, which can contribute to improve the crystallization rate due to its growth-dominated crystallization mechanism. Besides, a lower thermal conductivity for Zn$_{15}$Sb$_{85}$/SiO$_2$ multilayer materials may be another factor taken into account. So the multilayer Zn$_{15}$Sb$_{85}$/SiO$_2$ materials have good thermal stability as well as ultra-fast phase transition speed [27].

Fig. 7 (a) is an XRR diagram of the amorphous and crystalline states for the multilayer [ZS(3 nm)/SO(7 nm)]$_5$ materials. It can be seen that the Kiessig fringes and the total reflection edge move toward a higher angle after annealing at 280 °C for 5 min, indicating a decrease in thickness and an increase in mass density. The
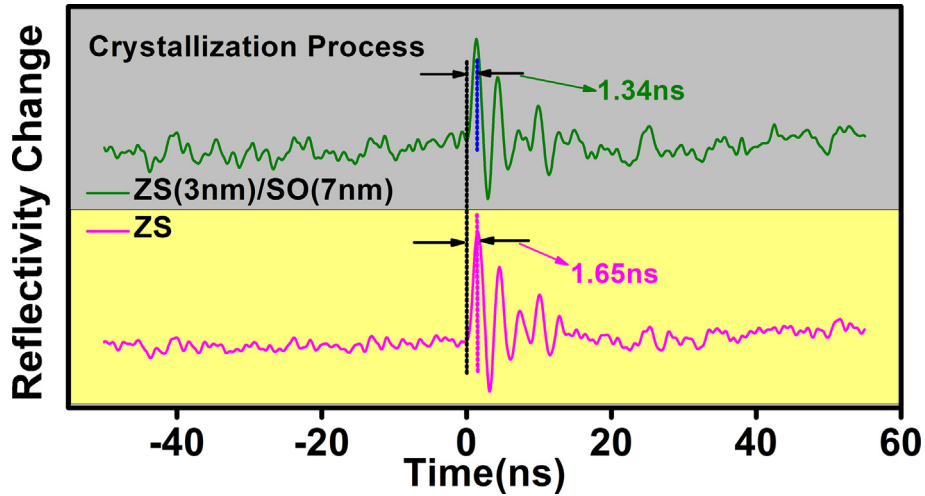
Fig. 6. Reflectivity evolutions in the crystallization process for the monolayer ZS and multilayer [ZS(3)nm/SO(7)nm]₅ materials.
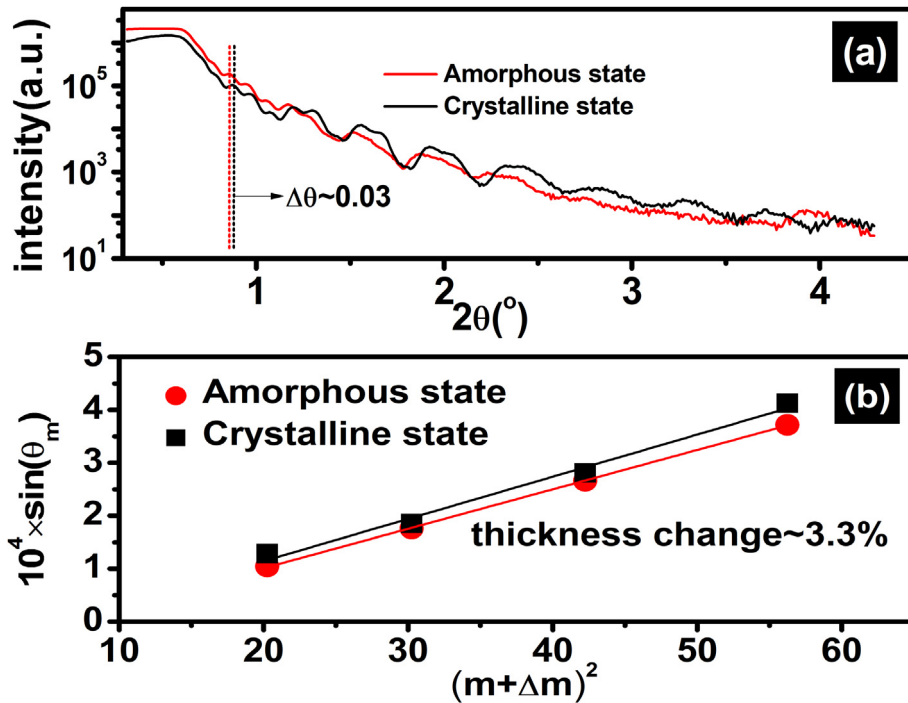

Fig. 7. (a) XRR patterns of the amorphous and crystalline [ZS(3)nm/SO(7)nm]₅; **(b)** plot of $\sin^2\theta_m$ versus $(m +\Delta m)^2$ for materials' thickness change.

thickness can be estimated according to the modified Bragg equation [28]:

$$\sin^2\theta_m = 2\delta + (m + 0.5)^2 \times (\lambda \div 2h)^2 \qquad (5)$$

Where δ, m ($m = 1, 2, 3 \ldots$), λ, t, and h are a constant, reflection series, wavelength of Cu-Kα radiation (0.154 nm), the thickness of materials, and correction factor, respectively [29]. Fig. 6(b) shows a plot of $sin^2\theta_m$ versus $(m + 0.5)^2$ for [ZS(3 nm)/SO(7 nm)]₅. It is noted that the value of reflection angle θ corresponds to the maximum intensity of the XRR pattern for each reflection series. The relationship between h and the slope of the fitted line (k) is given by

$$h = \frac{\lambda}{2\sqrt{k}} \qquad (6)$$

The thickness reduction upon crystallization of [ZS(3 nm)/ SO(7 nm)]₅ material was calculated to be only 3.3%, which was obtained from the slope of the modified Bragg fitting curves in Fig. 6(b). With the comparison of traditional monolayer GST materials (6.5%) [30], the multilayer [ZS(3 nm)/SO(7 nm)]₅ materials have the smaller thickness reduction. If the volume or density fluctuates is less, the better the adhesion will be, which avoids delamination of the phase change layer/electrode interface. Therefore, it is reasonable that the [ZS(3 nm)/SO(7 nm)]₅ has better reliability and reproducibility in multiple writing and erasing operations.

As shown in the inset of Fig. 8 (a), the structure of the fabricated device is a T-shaped mushroom-like PCM cell. The Al bottom electrode, the W heating electrode and the SiO₂ isolation layer were prepared by 130 nm complementary metal oxide semiconductor
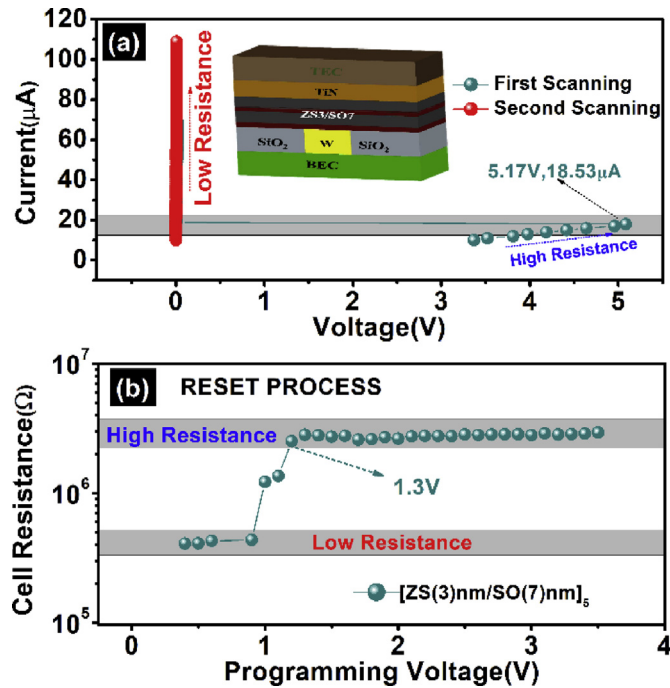
Fig. 8. **(a)** *I-V* curve of the PCM cells based on the multilayer [ZS(3)nm/SO(7)nm]$_5$ materials. Inset shows the Schematic diagram of a T-shaped mushroom-structured PCM cell. **(b)** *R-V* curve of the PCM cells based on [ZS(3)nm/SO(7)nm]$_5$.

technology. A 100 nm phase change layer of ZS/SO materials and a 20 nm TiN material were deposited on a semi-prepared cell by magnetron sputtering. The 200 nm Al layer was deposited as an upper electrode by ultra-high vacuum electron evaporation.

The SET operation using the DC scan mode is shown in Fig. 8(a). As the scan current increases, the voltage suddenly jumps back to a smaller value, which shows the threshold switching phenomenon and also indicates the transition of the device from amorphous to crystalline state [31]. The change in inter-band trap states in the amorphous phase with high electric fields had caused the threshold switching. According to Fig. 8(a), the threshold voltage (V_{th}) and the threshold current (i) are 5.17 V and 18.53 µA, respectively. When the current scan is carried out for the second time, the voltage is linearly proportional to the current, indicating the ohmic effect of resistance.

As seen in Fig. 8(b), the PCM cell can complete the reset operation within 100 ns Also the V_{RESET} of the ZS/SO is 1.3 V. By using the Joule heating equation $E_{RESET} = (V^2_{RESET}/R_{SET}) \times t_{RESET}$, the necessary energy for RESET operation of the PCM cell is calculated to be about 8.5×10^{-13} J with the 100 ns width pulse voltage, which is lower than the traditional GST cell (9.7×10^{-10} J) [32,33]. The lower the switching energy of the reset operation, the higher the set resistance and the faster the phase change speed. Lower power consumption facilitates the miniaturization and high density of PCM devices.

4. Conclusions

In this study, multilayer Zn$_{15}$Sb$_{85}$/SiO$_2$ materials have been investigated for PCM application. Among these, Zn$_{15}$Sb$_{85}$/SiO$_2$ materials have good thermal stability (Tc~230 °C, T_{10}~160 °C), fast phase change speed (crystallization time: 1.34 ns), high reliability (thickness change: 3.3%) and better stability (low surface roughness change). By comparing with GST, we can find that the [ZS(3 nm)/SO(7 nm)]$_5$ materials have better thermal stability, rapid switching

speed and better reliability. Also, T-shaped cells based on [ZS(3 nm)/SO(7 nm)]$_5$ achieves low RESET voltage (V_{RESET}~1.3 V). In summary, the multilayer Zn$_{15}$Sb$_{85}$/SiO$_2$ material is a promising candidate for PCM application.

References

[1] W.H. Wu, B. Shen, J.W. Zhai, X.Y. Liu, T.S. Lai, S.N. Song, Z.T. Song, Understanding the crystallization behavior and structure of titanium addition in germanium antimony phase change thin films, J. Mater. Chem. C. 10 (2018) 1039.
[2] Z.T. Song, S.N. Song, M. Zhu, L.C. Wu, K. Ren, W.X. Song, S.L. Feng, From octahedral structure motif to sub-nanosecond phase transitions in phase change materials for data storage, Sci. China Inf. Sci. 61 (2018), 081302.
[3] G.W. Burr, M.J. Brightsky, A. Sebastian, H.Y. Cheng, J.Y. Wu, S. Kim, N.E. Sosa, N. Papandreou, H.L. Lung, H. Pozidis, Recent progress in phase-change memory technology, IEEE J. Em. Sel.Top. C 6 (2016) 146–162.
[4] W.H. Wu, Z.H. Zhao, B. Shen, J.W. Zhai, S.N. Song, Z.T. Song, Crystallization characteristic and scaling behavior of germanium antimony thin films for phase change memory, Nanoscale 10 (2018) 7228–7237.
[5] A. Velea, F. Sava, G. Socol, A.M. Vlaicu, C. Mihai, A. Lőrinczi, I.D. Simandan, Thermal stability of phase change GaSb\GeTe, SnSe\GeTe and GaSb\SnSe double stacked films revealed by X-ray reflectometry and X-ray diffraction, J. Non-Cryst. Solids 492 (2018) 11–17.
[6] Y.H. Zheng, Y. Wang, T.J. Xin, Y. Cheng, R. Huang, P. Liu, M. Luo, Z.L. Zhang, S.L. Lv, Z.T. Song, S.L. Feng, Direct atomic identification of cation migration induced gradual cubic-to-hexagonal phase transition in Ge$_2$Sb$_2$Te$_5$, Chem. Commun. 2 (2019) 1–9.
[7] Y.H. Zheng, M. Xia, Y. Cheng, F. Rao, K. Ding, W. Liu, Y. Jia, Z. Song, S. Feng, Direct observation of metastable face-centered cubic Sb$_2$Te$_3$ crystal, Nano Res. 9 (2016) 3453–3462.
[8] K. Ren, M. Zhu, W.X. Song, S.L. Lv, M.J. Xia, Y. Wang, Y.Y. Lu, Z.G. Ji, Z.T. Song, Electrical switching properties and structural characteristics of GeSe-GeTe films, Nanoscale 11 (2019) 1595–1603.
[9] X. Chen, Y.H. Zheng, M. Zhu, K. Ren, Y. Wang, T. Li, G.Y. Liu, T.Q. Guo, L. Wu, X.Q. Liu, Y. Cheng, Z.T. Song, Scandium doping brings speed improvement in Sb$_2$Te alloy for phase change random access memory application, Sci. Rep. UK 8 (2018) 6839.
[10] S.Y. Chen, K. Yang, W.H. Wu, J.W. Zhai, Z.T. Song, Superlattice-like Sb-Ge thin films for high thermal stability and low power phase change memory, J. Alloys Compd. 738 (2018) 145–150.
[11] Y.H. Zheng, Y. Cheng, M. Zhu, X.L. Ji, Q. Wang, S.N. Song, Z.T. Song, W.L. Liu, S.L. Feng, A candidate Zr-doped Sb$_2$Te alloy for phase change memory application, Appl. Phys. Lett. 108 (2016), 052107.
[12] H. Zou, X.Q. Zhu, Y.F. Hu, Y.X. Sui, J.H. Zhang, Z.T. Song, Improving the thermal stability and phase change speed in Sb$_{70}$Se$_{30}$ films through Er doping, J. Mater. Sci. Mater. Electron. 28 (2017) 17719–17725.
[13] Y.H. Zheng, Y. Cheng, R.J. Huang, R. Qi, F. Rao, K.Y. Ding, W.J. Yin, S.N. Song, W.L. Liu, Z.T. Song, S.L. Feng, Surface energy driven cubic-to-hexagonal grain growth of Ge$_2$Sb$_2$Te$_5$ thin film, Sci. Rep. UK 7 (2017) 5915.
[14] W.L. Zhu, T. Wen, Y.F. Hu, X.Y. Liu, D. Gu, T.S. Lai, J.W. Zhai, Cycle number manipulating effect on crystallization temperature of superlattice-like [Ge/Ge$_8$Sb$_{92}$]n phase-change films, J. Alloys Compd. 723 (2017) 936–941.
[15] L. Wang, J. Wen, B. Xiong, Nanoscale thermal cross-talk effect on phase-change probe memory, Nanotechnology 29 (2018) 375201.
[16] G.X. Wang, Y.W. Zhang, P. Liu, J.X. Wang, Q.H. Nie, X. Shen, Phase change behavior of pseudo-binary ZnTe-ZnSb material, Mater. Lett. 213 (2018) 342–345.
[17] Z.F. He, S.Y. Chen, W.H. Wu, J.W. Zhai, S.N. Song, Z.T. Song, Investigation of multilayer SnSb$_4$/ZnSb thin films for phase change memory applications, Appl. Phys. Exp. 10 (2017), 055504.
[18] W.H. Wu, S.Y. Chen, J.W. Zhai, Study on the physical properties and structure of titanium antimony thin films for phase change memory application, J. Mater. Sci. 52 (2017) 11598–11607.
[19] H.P. You, Y.F. Hu, X.Q. Zhu, H. Zou, S.N. Song, Z.T. Song, Investigation of Cu–Sn–Se material for high-speed phase-change memory applications, J. Mater. Sci. Mater. Electron. 28 (2017) 10199–10204.
[20] Y.F. Hu, X.Q. Zhu, H. Zou, L. Zheng, S.N. Song, Z.T. Song, O-doped Sb materials for improved thermal stability and high-speed phase change memory application, J. Alloys Compd. 696 (2017) 150–154.

[21] Y.F. Hu, X.Q. Zhu, H. Zou, H.Y. You, L.J. Zhai, S.N. Song, Z.T. Song, Nanosecond switching in superlattice-like GeTe/Sb thin film for high speed and low power phase change memory application, ECS J. Solid State SC 6 (2017) 45–48.

[22] L.C. Zhang, N.H. Miao, J. Zhou, J.X. Mi, Z.M. Sun, Insight into the role of W in amorphous GeTe for phase-change memory, J. Alloys Compd. 738 (2017) 270–276.

[23] G.Y. Liu, L.C. Wu, M. Zhu, Z.T. Song, F. Rao, S.N. Song, Y. Cheng, The investigations of characteristics of Sb_2Te as a base phase-change material, Solid State Electron. 135 (2017) 31–36.

[24] H. Zou, X.Q. Zhu, Y.F. Hu, Y.X. Sui, L. Zheng, W.H. Wu, L.J. Zhai, J.Z. Xue, Z.T. Song, Superlattice-like $Ga_{40}Sb_{60}$/Sb films with ultra-high speed and low power for phase change memory application, J. Mater. Sci. Mater. Electron. 28 (2017) 3806–3811.

[25] R.R. Liu, P.Z. Wu, Z.F. He, J.W. Zhai, X.Y. Liu, T.S. Lai, Study of crystallization and thermal stability of superlattice-like $SnSb_4$-GeTe thin films, Thin Solid Films 625 (2017) 11–16.

[26] Z.F. He, W.H. Wu, X.Y. Liu, J.W. Zhai, T.S. Lai, S.N. Song, Z.T. Song, Improvement of phase change properties of stacked $Ge_2Sb_2Te_5$/ZnSb thin films for phase change memory application, Mater. Lett. 185 (2016) 399–402.

[27] Y. Shuang, Y. Sutou, S. Hatayama, S. Shindo, Y.H. Song, D. Ando, J. Koike, Contact resistance change memory using N-doped $Cr_2Ge_2Te_6$ phase-change material showing non-bulk resistance change, Appl. Phys. Lett. 112 (2018) 183504.

[28] Y.G. Lu, S.N. Song, X.Y. Shen, Z.T. Song, G.X. Wang, S.X. Dai, Study on phase change properties of binary GaSb doped Sb-Se film, Thin Solid Films 589 (2015) 215–220.

[29] H.P. You, Y.F. Hu, T.S. Lai, Q.Q. Chou, X.Q. Zhu, H. Zou, High thermal stability and low power dissipation PCM with nanoscale oxygen-doped SS thin film, IET Nanobiotechnol. 12 (2018) 1080–1083.

[30] M. Bouska, S. Pechev, Q. Simon, R. Boidin, V. Nazabal, J. Gutwirth, E. Baudet, P. Nemec, Pulsed laser deposited GeTe-rich GeTe-Sb_2Te_3 thin films, Sci. Rep. UK 6 (2016) 26552.

[31] Y. Wang, T.Q. Guo, G.Y. Liu, T. Li, S.L. Lv, S.N. Song, Y. Cheng, W.X. Song, K. Ren, Z.T. Song, Sc-centered octahedron enables high-speed phase change memory with improved data retention and reduced power consumption, ACS Appl. Mater. Interfaces 11 (2019) 10848–10855.

[32] Q.Q. Zheng, T.Q. Guo, L.L. Chen, S.N. Song, X. Zhang, W.L. Yu, X.W. Zhu, H.H. Shao, W.T. Zheng, J. Zhang, Effect of copper doping on the crystallization behavior of TiSbTe for fast-speed phase change memory, Mater. Lett. 241 (2019) 148–151.

[33] Z.G. Li, Y.G. Lu, M. Wang, X. Shen, X.H. Zhang, S.N. Song, Z.T. Song, Controllable multilevel resistance state of superlattice-like GaSb/Ge_2Te films for ultralong retention phase-change memory, J. Non-Cryst. Solids 481 (2018) 110–115.